RESEARCH ARTICLE

Ultra-High Extinction Dual-Output Thin-Film Lithium Niobate Intensity Modulator

SEAN P. NELAN [1,2], ANDREW MERCANTE[2], SHOUYUAN SHI[1,2], PENG YAO[2],
ELIEZER SHAHID [2], BENJAMIN A. SHOPP[2], COOPER D. HURLEY[1], MATHEW ZABLOCKI[2],
AND DENNIS W. PRATHER[1,2]
[1]School of Electrical and Computer Engineering, University of Delaware, Newark, DE 19716, USA
[2]Phase Sensitive Innovations, Newark, DE 19713, USA

Corresponding author: Sean P. Nelan (snelan@udel.edu)

ABSTRACT A low voltage, wide bandwidth compact electro-optic modulator is a key building block in the realization of tomorrow's communication and networking needs. Recent advances in the fabrication and application of thin-film lithium niobate, and its integration with photonic integrated circuits based in silicon make it an ideal platform for such a device. In this work, a high-extinction dual-output folded electro-optic Mach Zehnder modulator in the silicon nitride and thin-film lithium niobate material system is presented. This modulator has an interaction region length of 11 mm and a physical length of 7.8 mm. The device demonstrates a fiber-to-fiber loss of roughly 12 dB using on-chip fiber couplers and DC half wave voltage (Vπ) of less than 3.0 V, or a modulation efficiency (Vπ·L) of 3.3 V·cm. The device shows a 3 dB bandwidth of roughly 30 GHz. Notably, the device demonstrates a power extinction ratio over 45 dB at each output port without the use of cascaded directional couplers or additional control circuitry; roughly 31 times better than previously reported devices. Paired with a balanced photo-diode receiver, this modulator can be used in various photonic communication systems. Such a detecting scheme is compatible with complex modulation formats such as differential phase shift keying and differential quadrature phase shift keying, where a dual-output, ultra-high extinction device is fundamentally paramount to low-noise operation of the system.

INDEX TERMS Lithium niobate, modulator, thin-film, electro-optic, extinction, link.

I. INTRODUCTION

The systems that support the world's communication networks are showing their age [1]. In the last decade, global data traffic has and continues to grow exponentially while existing infrastructure is becoming more costly, less efficient and less reliable as its capability is overextended [1], [2], [3]. An urgency is now placed on network providers to enhance networks and meet greater demands [3], [4]. At the forefront of high-speed networking is the need to transmit data to networking hubs efficiently and reliably over long distances without the need for in-line amplification or repeater stations [5]. Existing coaxial cables are heavy, lossy and make long range data transmission difficult [6]. In turn, the shift to optical fiber-based transmission has become more desirable.

The associate editor coordinating the review of this manuscript and approving it for publication was Weiren Zhu .

Here, the optical modulator is used to overlay an electrical signal onto an optical signal for long range transmission through an optical fiber, be it to an antenna atop a radio tower, or to a networking hub hundreds of miles away [5]. The optical modulator is an integral part of active and passive millimeter wave imaging systems, modern telecommunications networks and data communication, and is widely used in on-chip RF photonic devices, frequency comb generation, on chip signal splitting, sensing, and quantum photonics [1], [4], [7], [8], [9], [10], [11], [12], [13], [14], [15], [16], [17], [18], [19], [20], [21], [22], [23], [24].

If an optical modulator is to be integrated with existing systems, it should maintain a small device footprint, feature a wide RF bandwidth and remain environmentally stable for reliable operation in any environment [14], [15], [16], [21], [25]. Moreover, the ideal optical modulator boasts a high (>35dB) extinction ratio [8], [10], [14], [26], [27]. At first

glance, Si-based free carrier plasma dispersion-based modulators would seem the ideal candidate, but their low cost and excellent scalability is overshadowed by poor extinction ratio and bandwidth; an inherent limitation of a dispersion-based modulation scheme [17], [28], [29]. Si-based modulation is further blighted by high intrinsic absorption loss, narrow transmission spectrum and dopant diffusion at high temperatures [14], [17]. Finally, because Si is a centrosymmetric material, it demonstrates a high third-order non-linearity and a low second-order non-linearity, which excludes it from efficient operation at high optical powers [30]. While the integration of organic electro-optic polymers with the Si platform has been shown to mitigate some of its inherent drawbacks, the organic nature of the platform does not lend itself to long-term environmental stability [11], [22], and [31].

Si-based free carrier plasma dispersion-based modulation platform is then ruled out in favor of lithium niobate-based modulation, where the ideal platform for a low-voltage, high-bandwidth and environmentally-stable modulator should show a strong electro-optic (Pockels) effect, and a linear response to an applied modulation voltage irrespective of the optical power and wavelength [8], [12], [15], [16], [21], [25]. Lithium niobate ($LiNbO_3$) brings an extremely strong second-order non-linearity ($\chi^{(2)}$), a strong linear electro-optic effect, low optical absorption across a wide range of wavelengths, pure phase modulation, zero chirping and exceptional stability at high temperatures [8], [15], [25]. $LiNbO_3$, with its trigonal crystal system, lacks inversion symmetry and boasts a third-order non-linearity ($\chi^{(3)}$) which is three magnitudes lower than Si [8], [30].

Commercial, or bulk $LiNbO_3$ modulators use titanium (Ti)-diffused waveguides to carry the optical mode, but suffer poor optical confinement ($\Delta n < 0.02$) which results in a large optical mode size [8], [25]. This requires metal electrodes to be placed far from the optical waveguide to avoid metal absorption loss, and results in large bending radii. Consequentially, the Vπ and the size of the device is increased. A typical commercial $LiNbO_3$ modulator brings a Vπ·L of 12-32 V·cm [12], [21], [25].

Recently, advances in crystal ion sliced (CIS) films of $LiNbO_3$ on insulator (TFLNOI), which guide optical modes almost 20 times smaller than their bulk-$LiNbO_3$ counterparts have emerged as an answer to some of these issues [8], [15], [16], [25], [32], [33]. Now, strip-loaded waveguides can be used to tightly confine the optical mode, allowing smaller electrode gaps, decreased Vπ, tighter bending radii and photonic integrated circuit (PIC) compatibility. In previous work, ultra-wide bandwidth, high efficiency and low loss modulators have been demonstrated in the TFLNOI material system with ridge-etched and strip-loaded waveguides [8], [14], [15], [25]. To facilitate the use of a mode-transition coupler at the input and output of the device, silicon nitride (SiN_x) was again chosen as the ideal candidate to create a strip loaded waveguide in the TFLNOI platform. SiN_x has low propagation loss across telecom optical wavelengths, high power handling capability and a similar optical index

to $LiNbO_3$ [5], [34], [35], [36], [37]. SiN_x also features a low third-order non-linearity, small thermo-optic coefficient, and can be deposited using plasma enhanced chemical vapor deposition (PECVD) [5], [34], [35], [36], [37].

One must also consider the packaging and size of the device. A conventional push-pull electro-optic modulator utilizes a straight waveguide before and after the interaction region, where light enters one side of the device and exits the opposite side, requiring fiber coupling to both sides of the device simultaneously [15], [25], [32]. To reduce the size, weight, power and cost (SWaP-C) of the system, the device can be "folded." Here, a 180° bend is introduced to the waveguides and electrodes to direct the signal back towards the input. Now, the length of the device is halved with no adverse affect on modulation efficiency or bandwidth [8], [38], [39]. The modulator can then be used with a single, easily packaged v-groove array (VGA), can be folded multiple times with little impact to the overall footprint, and only requires the polishing and preparation of one end-facet [8], [39]. However, this layout does introduce some challenges to the design and fabrication of the modulator. If a standard Mach-Zehnder Modulator (MZM) were to be bent back on itself such that the interaction regions before and after the bend were the same length, the latter region would reverse any modulation imparted by the first, because the polarity of the modulating electric field interacting with the mode inside the $LiNbO_3$ is now the inverse of what it was during the first half of the modulator [8], [38], [39]. Moreover, the optical path lengths of the inner and outer interaction regions would be mismatched, and the device would show a frequency-dependent response.

In previous work, a waveguide crossing was used to ensure both sections of the modulator, before and after the fold, contribute to the total modulation of the device [8]. A crossing is again used in this device to minimize the overall footprint. The optical path length of both arms, and the optical vs. electrical path length is then matched to allow operation without any wavelength-dependent effects or RF and optical field separation. A symmetric 2 × 2 multi-mode interference (MMI) splitter is placed at the output of the device to yield two outputs with intensities inversely proportional to each other. Paired with a balanced photo-diode (PD) receiver, a dual-output MZM can be used in many RF photonic link systems that require an extremely low noise floor and spurious-free dynamic range (SFDR) performance. This is vital to communication systems and enables heavy, lossy and space-consuming cables to be replaced with light, almost lossless and small volume optical fibers [6]. A dual-output MZM/balanced PD receiver pair is capable of detecting not only the signal amplitude, but also the phase information. As a result, such detecting scheme is compatible with complex modulation formats such as differential phase shift keying (DPSK) and differential quadrature phase shift keying (DQPSK) [40].

Through careful design of input and output splitters, and the use of symmetric MMI splitters, an extinction ratio over
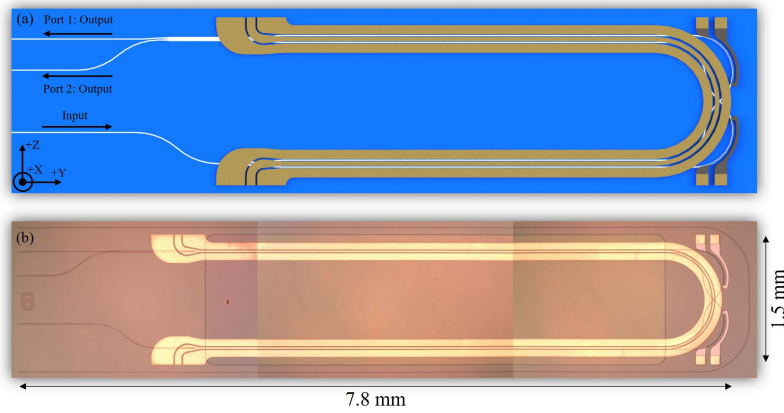
FIGURE 1. (a) Aerial view of a rendering of the folded modulator with waveguide crossing showing crystal axis and device port direction. (b) Aerial view of the fabricated folded modulator with waveguide crossing.

45 dB is achieved at each output port. This design does not require cascaded directional couplers and additional control circuitry to control splitting imbalance, but the optical loss in both waveguides in the interaction region of the modulator must be closely matched through careful fabrication to achieve the high extinction ratio [26]. This will be discussed later in the work. The measurement shows repeatability across multiple devices.

In this work, a high extinction ratio hybrid $LiNbO_3$-SiN_x electro-optic MZM with two equal and opposite outputs is designed, fabricated and characterized. Fiber couplers are used at the input and output to lower the total insertion loss to 12 dB. To the best of our knowledge, this is the first time a high extinction ratio, folded, $LiNbO_3$-SiN_x dual-output MZM with a waveguide crossing has been demonstrated in this material platform. The device presented shows a measured DC-$V\pi$ of 3.0 V with an 11 mm interaction region, and an extinction ratio of over 45 dB.

II. DESIGN AND SIMULATION
A. DEVICE LAYOUT
The 3D aerial view of the folded electro-optic modulator, including thermal biasing heaters is shown in Fig. 1. (a) and (b). The electrode contains one interaction region before and after the folded region, each 5.5 mm long. The input and output ports are defined in Fig. 1. (a). The material stack, from top to bottom, is comprised of a 450 nm buffer layer of PECVD SiO_2 (T_{BUF}), 100 nm of PECVD SiN_x deposited on 300 nm X-cut thin-film $LiNbO_3$, which is bonded to a 4.7 μm SiO_2 layer (T_{BBUF}), atop a 500 μm Si handle. To efficiently guide the first order transverse electric (TE) mode, the width (W_{SiN}) and thickness (T_{SiN}) of the strip-loaded single-mode SiN_x waveguide is chosen to be 2 μm and 100 nm, respectively. The simulated fundamental TE mode in the interaction region of the device can be seen in Fig. 2. (a). The waveguide cross section in the interaction region and material stack are defined in Fig. 2. (c) and (d),
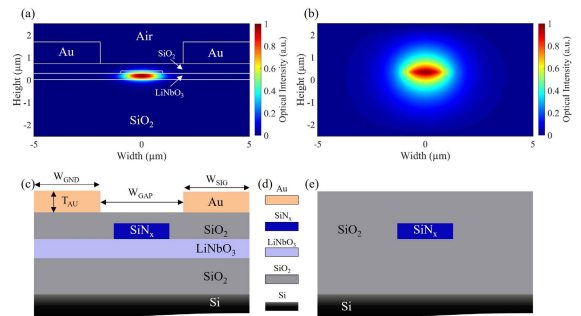

FIGURE 2. (a) Simulated mode field of the waveguide in the interaction region. Simulations done in Lumerical MODE Solver. (b) Simulated mode field of the waveguide at the end facet. Simulations done in Lumerical MODE Solver. (c) Cross-sectional view of a single arm of the material structure in the interaction region. Dimensions are labeled. (d) Material definitions. (e) Cross-sectional view of the material structure at the device end facet.

respectively. The device uses a fiber coupler at the end facet to minimize free-space coupling loss caused by the mode field diameter (MFD) mismatch between the lensed fiber and the waveguide. The mode field in the fiber coupler can be seen in Fig. 2. Here, the $LiNbO_3$ film is etched away from the end facets of the sample, where the optical mode travels in a SiN_x strip clad in SiO_2 to closely match the MFD of the fiber (b). This reduces the optical coupling loss at each end facet from roughly 7 dB per facet to nearly 2 dB per facet. The optical mode propagates in the Y-crystal direction, while the electrodes are placed such that the RF field is polarized in the +/− Z-crystal direction, where the maximum $r_{33} =$ 31 pm/V coefficient is achieved for the TE optical mode [5], [8], [25], [35], [41]. The layout and design of the folded modulator with a waveguide crossing are further discussed in previous work where a standard single output folded MZM is reported [8].

A 2 × 2 MMI splitter that recombines the light to produce an intensity-modulated signal is deployed on the output of the

device. The symmetric 2 × 2 multi-mode interference (MMI) splitter yields two outputs which are inversely proportional to each other. When the device is biased such that one output is at it's peak intensity, the other output is at it's lowest, or null intensity. The device can then be paired with a balanced PD receiver to eliminate any common-mode noise between both outputs [42].

B. 2 × 2 MMI SPLITTER DESIGN

An MMI splitter and combiner are used as 3 dB couplers to both split and recombine light before and after the interaction region of the device, respectively. Directional couplers and Y-splitters which require an extremely small gap between waveguides are sensitive to fabrication errors [26]. The MMI offers greater fabrication tolerance, and in the case of the 1 × 2 MMI, the symmetric design does not require precise, sub-micron accuracy of device length to maintain an equal splitting ratio [25], [43]. The design, simulation and fabrication of the 1 × 2 MMI splitter is reported in previous work [8].

To achieve an inversely-proportional, balanced output from the MZM, a 2 × 2 MMI is used at the output of the device following the interaction region. The 2 × 2 MMI operates based on the self-imaging principle, where any input field is reconstructed periodically after a certain propagation distance [43]. With this in mind, the length (L_{MMI}) of the 2 × 2 MMI must be designed such that the input field from either port is reconstructed into two output fields at the end of the device. The width of the MMI is then set to 15 μm to avoid evanescent coupling of the output fields after the multimode region. The mode separation distance (S_{MMI}) is 8 μm between both ports of the 2 × 2 MMI.

The initial length of the multimode waveguide region is estimated using the 2D mathematical approximation given by [25], [43], [44]:

$$L_{MMI} = \frac{4 n_r w_e^2}{N \lambda_0}. \tag{1}$$

Here, n_r is the effective index of the multimode region, w_e is the width of the multimode region (W_{MMI}), N is the number of self-images (inputs and outputs), and λ_0 is the input wavelength in vacuum. The n_{eff} of the lowest order TE modes in the MMI region are found to be 2.128018, and 2.129952, respectively, using Lumerical's MODE solver. This results in a multimode region length of 618 μm. For optimization of the initial design parameters, Lumerical's MODE simulation software is used. With $W_{MMI} = 15\ \mu$m and $S_{MMI} = 8\ \mu$m, the final length of the structure is found to be $L_{MMI} = 640\ \mu$m, which is very close to the length given by the self-imaging method. For further reduction of the mode-index mismatch between the MMI region and the input waveguide, linear tapers of length (L_{TPR}) 52.5 μm and width (W_{TPR}) 7 μm are introduced at the input and output section, shown in Fig. 3. (d). The introduction of a taper increases the range of MMI lengths over which it continues to split the input mode equally among the two outputs as well as the bandwidth of the
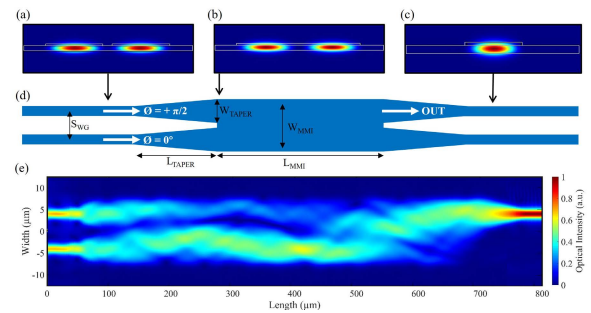

FIGURE 3. (a) Mode field cross section in the input waveguides of the 2 × 2 MMI when both input ports are illuminated with a $\pi/2$ phase difference. (b) Mode field cross section at the input of the 2 × 2 MMI when both input ports are illuminated with a $\pi/2$ phase difference. (c) Mode field cross section at the output of the 2 × 2 MMI when both input ports are illuminated with a $\pi/2$ phase difference. (d) Aerial rendering of the 2 × 2 MMI. Dimensions and port propagation directions are labeled. (e) Mode cross section in the +X crystal axis of the 2 × 2 MMI when both input ports are illuminated with a $\pi/2$ phase difference. Propagation occurs from left to right.

MMI, which is wavelength-dependent as the 3 dB coupling length depends on $\frac{1}{\lambda}$ [8], [25], [45]. Using Lumerical's FDTD simulation software, the optimized length of the MMI with tapered input and output ports is found to be $L_{MMI} = 636\ \mu$m. This is near the length given by the self-imaging equation, but the introduction of linear tapers has an effect on the overall length of the cavity to properly reconstruct the image at the output waveguides, and slightly reduces the multimode region length. Because both the 1 × 2 and the 2 × 2 MMI are symmetrically fed when both input ports are illuminated, the input power should be equally split among the output arms barring any fabrication intolerance. This will be confirmed later in the manuscript through measuring the extinction ratio at each port. An electric field profile for the designed two-fold self-image MMI is shown in Fig. 3. (e).

C. TRAVELING WAVE ELECTRODE DESIGN

The ground-signal-ground (GSG) co-planar waveguide (CPW) electrodes must maintain a 50 Ω impedance at the high-frequency operation limit of the device with minimal RF absorption or conduction loss to minimize reflections in the feed network. The dimensions of the GSG electrodes are defined in Fig. 2. (c). The electrode gap (W_{GAP}) must be kept as small as possible to maximize RF and optical field overlap, contributing to low-voltage operation, but must not contribute to excess optical absorption loss from the TE mode interacting with the Au electrode [8], [15], [25], [27]. In Fig. 4, the simulated $V\pi{\cdot}L$ is plotted against W_{GAP} and T_{BUF}. To achieve a $V\pi{\cdot}L$ of roughly 3.3 V·cm, or a $V\pi$ of roughly 3 V with our 11 mm interaction region, W_{GAP} is set to 4 μm and T_{BUF} is set to 450 nm. This yields an additional optical absorption loss of roughly .08 dB/cm. The width of the ground electrodes (W_{GND}) is set to 75 μm, and the height of the electroplated Au electrodes (T_{ELEC}) is 1 μm. The optimal electrode signal width (W_{SIG}) is found to be 24.5 μm using Ansys High Frequency Structure Simulator
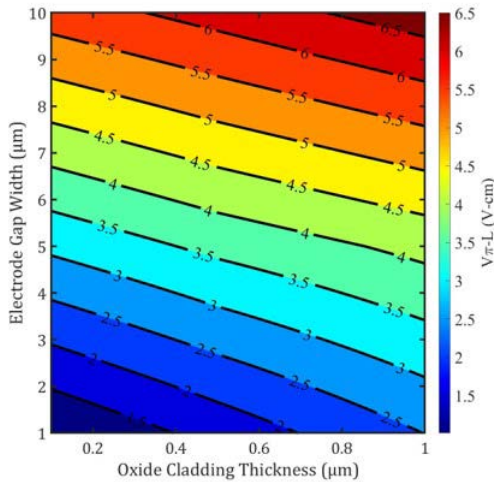
FIGURE 4. The effect of electrode gap width (W_{GAP}) and oxide cladding thickness on $V\pi \cdot L$.

(HFSS), in a process described in previous work [8]. An index matching fluid (UV15) is applied to the GSG electrodes in the interaction region and fold to more closely match the RF and optical group velocities and improve modulation bandwidth [8], [14], [15], [46].

The high frequency electrical response of the GSG electrodes is characterized through a 2-port measurement using a Keysight PNA-X network analyzer. A 50 Ω GSG probe is connected to each end of the GSG electrodes, and a frequency sweep performed from 0 to 40 GHz. The measured air-clad and UV15-clad S-parameters are plotted in Fig. 5 (a) and (b), respectively. At 40 GHz, S(2,1) is observed to be roughly -3 dB and -4 dB at the 40 GHz target frequency for the air-clad and UV15-clad electrode, respectively. There is a periodic resonance seen in S(1,1) and S(2,2), which is caused by constructive and destructive interference from reflections at the probe points as the frequency is swept. The RF impedance with and without index matching fluid is plotted in Fig. 5. (d). The observed resonance of the electrode is seen in the measured impedance. The RF group index (n_{RF}) with and without index matching fluid is plotted alongside the optical group index (n_{Og}) in Fig. 5 (c). The n_{Og} of the fundamental TE mode is found to be roughly 2.14, while the group index of the RF mode in the air-clad and UV15-clad electrodes (n_{RF}) is roughly 1.85 and 2.10, respectively. The index mismatch between the optical and RF mode is then 0.04 with index matching fluid, with the RF mode propagating faster than the optical mode.

III. FABRICATION

Fabrication of the folded modulator begins on a 300 nm thick X-cut TFLNOI substrate procured from NanoLN™. A 4.7 μm layer of thermal SiO_2 below the $LiNbO_3$ is bonded to a 500 μm thick Si handle. Electron-beam lithography (EBL) is used to pattern alignment structures in TiW (10%/90%) for future lithographic steps. A 100 nm thick

layer of SiN_x is deposited on top of the thin-film $LiNbO_3$ using PECVD. This layer will be used to define the SiN_x strip-loaded waveguides. The refractive index for the SiN_x is 1.943 at 1550 nm. EBL is again used to define the optical structures. The features are defined via dry etching of the SiN_x layer in an inductively coupled plasma (ICP). A 2 μm SiO_2 buffer layer is then deposited using PECVD. A laser writer is used to pattern the regions where an increased thickness of the SiO_2 buffer layer will protect the optical mode from interacting with an overhead Au electrode. The rest of the SiO_2 buffer layer is reduced to 450 nm thickness via dry etching in an ICP. To reduce RF absorption losses, the device is annealed in an O_2 environment. A seed layer is deposited onto the sample using an Angstrom metal sputtering system and the electrodes are defined via EBL. An electroplating process is then used to realize the 1 μm thick Au electrodes. Finally, the device's waveguide facets are polished to increase fiber coupling efficiency. A simplified flow of the fabrication steps is found in Fig 6. An image of the fabricated modulator is shown in Fig. 1. (b). This process is expanded upon in previous work [8].

IV. OPTICAL AND RF CHARACTERIZATION

A. OPTICAL LOSS CHARACTERIZATION

A tunable telecom laser (Keysight 81608A) is used at a wavelength of 1550 nm and connected to an OZ Optics 1 × 4 lensed fiber array, with a mode field diameter (MFD) of roughly 2.5 μm through a polarization-maintaining (PM) fiber patch cable. The laser output from the lensed fiber array is free-space coupled to the on-chip fiber coupler. Due to the MFD mismatch between the lensed fiber and on-chip coupler, there is a 4.44 dB coupling loss per facet. Now, the tunable laser source is replaced with a reflectometer/lightwave analyzer (Luna OBR 6415), and the optical back-scatter and propagation loss from a reference structure is measured and shown in Fig. 7. (d) to be. 64 dB/cm. The total insertion loss of the device is roughly 12.0 dB. The on-chip loss after the 17 mm path length is roughly 1.1 dB. This accounts for roughly 9.98 dB total insertion loss. The additional 2.02 dB loss is incurred due to the difference in extension between the lensed fibers in the lensed fiber array, preventing proper free-space fiber alignment. In future work, the on-chip fiber coupler can be made to work with a flat-polished v-groove array (VGA), to eliminate losses from fiber array alignment.

B. 2 × 2 MMI INPUT RESPONSE CHARACTERIZATION

The 2 × 2 MMI must provide two arms with inversely proportional field intensities, varying with the phase difference between both input ports if it is to be used in a MZM configuration for a balanced link. Because one output of the ideal 2 × 2 MMI contains a $\frac{\pi}{2}$ phase shift with respect to the other when fed through one input arm, and considering the reciprocal nature of the device, illuminating both input arms with phase shift of π enables switching of light from one port to the other port. We can use the field transfer matrix of a 2 × 2
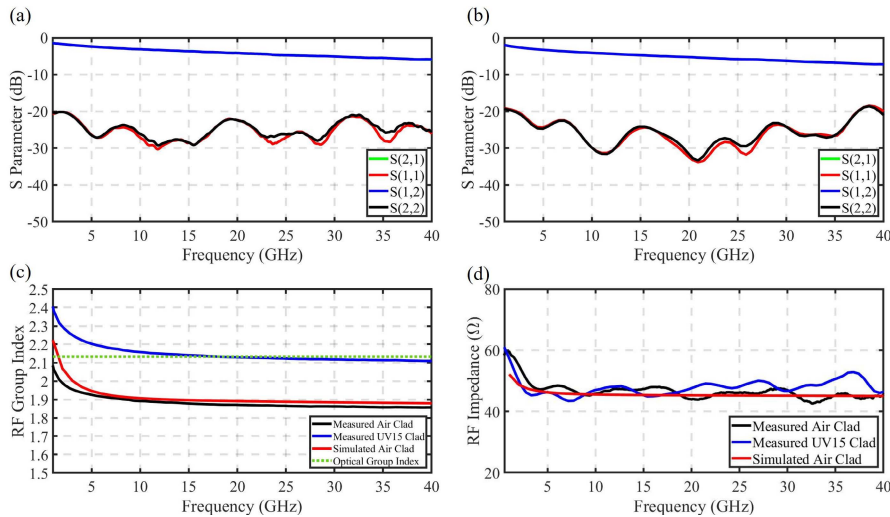
FIGURE 5. (a) Measured S-parameters of the air-clad CPW GSG electrodes from 0 to 40 GHz. Extracted from the real and imaginary measured S-parameter matrix. (b) Measured S-parameters of the UV15-clad CPW GSG electrodes from 0 to 40 GHz. Extracted from the real and imaginary measured S-parameter matrix. (c) RF group index of the GSG electrodes from 0 to 40 GHz. Extracted from the real and imaginary S(2,1) parameters. (d) RF impedance of the GSG electrodes from 0 to 40 GHz. Extracted from the real and imaginary S(1,1) parameters.
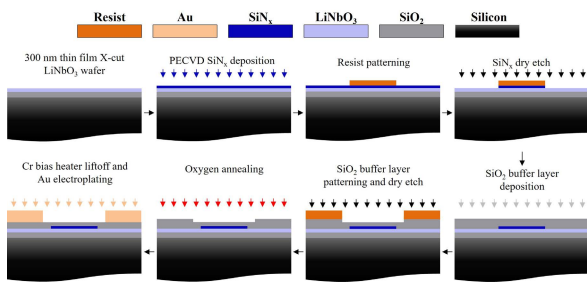

FIGURE 6. Simplified fabrication flow chart of the folded SiN$_x$-LiNbO$_3$ modulator.

MMI, shown in Eq. (2), to show the relationship between the difference in phase between the two input arms ($\Delta\phi$), and the transmission through each output arm [19]:

$$\begin{bmatrix} A' \\ B' \end{bmatrix} = e^{j\phi_0} \begin{bmatrix} 1 & e^{\frac{j\pi}{2}} \\ e^{\frac{j\pi}{2}} & 1 \end{bmatrix} \begin{bmatrix} A \\ B \end{bmatrix}. \qquad (2)$$

The power transferred through each arm is modeled using $\frac{|A'|^2}{2}$ and $\frac{|B'|^2}{2}$. In Fig. 7. (b), it is confirmed that the MMI can maintain an equal splitting ratio across a range of optical wavelengths, where a peak splitting difference of 1.4% is found at the 1530 nm input wavelength. This still supports an ER of over 40 dB, shown later in this work. In Fig. 7. (c), the same relationship is demonstrated using Lumerical's FDTD simulation software. Here, two Gaussian mode sources are applied to the inputs of the structure, while one's phase is swept from 0 to 2π radians. The normalized power transmission through each output arm is plotted along this sweep.

An imbalanced Mach-Zehnder Interferometer (MZI) is constructed from a directional fiber coupler, where a tunable

laser source is equally split among two fibers of lengths 1 m and 1.5 m, and then connected to a 1×2 OZ Optics v-groove array (VGA), aligned to launch TE-polarized light at 1550 nm. The VGA is aligned to the input waveguides of the 2×2 MMI. An identical VGA is aligned to the output waveguides of the device and each fiber is fed to a broadband InGaAs photodetector before being directed to an oscilloscope. The laser source is swept from 1549.9 nm to 1550.1 nm at 10 nm/s, at a step length of 0.1 nm. Because there is a length difference in the fibers after the 3 dB directional coupler and before the MMI, sweeping the laser source creates a periodic phase variation among the input ports of the MMI. The output power of each port is then captured simultaneously on the oscilloscope and can be seen in Fig. 7. (a). Here, an inversely proportional optical intensity between both device's output ports is experimentally validated. The same experiment is performed in Lumerical FDTD and shown in Fig. 7. (c). Here, both inputs of the device are illuminated with an equal optical intensity, and an input phase sweep is performed to show that an inversely proportional relationship between the optical intensity at the output ports exists.

C. DC RESPONSE CHARACTERIZATION

The MZM functionality as an electro-optic (EO) transducer is measured at low frequencies and plotted in Fig. 7. (f). The observed Vπ is our chosen figure-of-merit (FOM). A low speed (150 kHz) triangular voltage wave is applied to the GSG electrodes using an arbitrary waveform generator via a GSG probe. The device's electrodes are excited such that the center electrode is active, while the outer electrodes are grounded. The optical output signal from each output port is connected to a broadband photodetector, which is
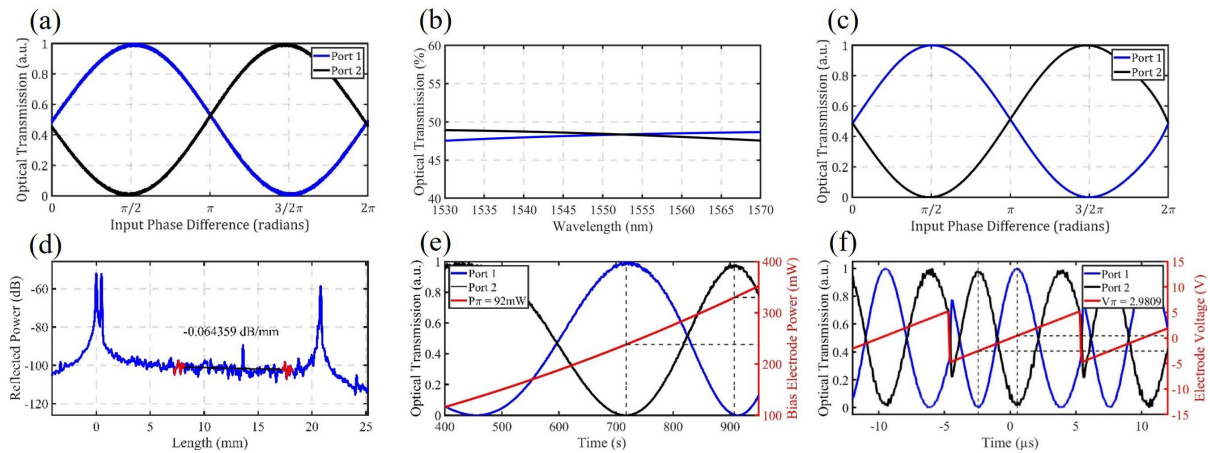
FIGURE 7. (a) Reference 2 × 2 MMI transmission in each output port vs phase difference between each input port. Data experimentally collected. (b) Simulated 2 × 2 MMI transmission in each output port vs input wavelength across optical C-band. Peak splitting difference is 1.4%. (c) Reference 2 × 2 MMI transmission in each output port vs phase difference between each input port. Data simulated in ANSYS Lumerical FDTD. (d) Measured propagation loss of the on-chip reference structure. Measured propagation loss is 0.64 dB/cm. (e) Measured optical power of the folded modulator at each output port vs power applied to the thermal bias electrode. $P\pi = 92$ mW. (f) Measured optical power of the folded modulator at each output port vs voltage applied to the RF GSG electrodes. $V\pi = 2.98$ V.

connected to an adjustable trans-impedance amplifier (TIA) and connected to an oscilloscope. The output of the arbitrary waveform generator and photodetectors are observed on the oscilloscope and presented in Fig. 7. (f). The measured $V\pi$ agrees with the simulated value of roughly 3 V.

The same experiment is then performed using a thermo-optic (TO) phase shifter near the fold of the device to ensure the device can be biased to null, quadrature and peak bias. The input power is swept from 100 mW to 350 mW and the output of both photodetectors is plotted alongside the applied TO phase shifter power in Fig. 7. (e). The power required to shift from null to peak bias ($P\pi$) is found to be $P\pi = 92$ mW.

D. EXTINCTION RATIO CHARACTERIZATION

Through careful design of the 2 × 2 MMI splitter/combiner used at the output of the device, the optical extinction ratio can be improved compared to previous work which employs a 2 × 1 MMI combiner [8]. When a 2 × 1 MMI is used at the output of an MZM, and the MZM is biased to a null condition such that there is a π phase difference between both modulation arms, the light entering the 2 × 1 MMI will interfere destructively at the output port and create substrate modes in the LiNbO$_3$ slab. While very little light may immediately enter the output waveguide, a portion of optical power from the substrate modes will couple back into the waveguide after some length, leading to a degraded extinction ratio.

To solve this, we have placed a 2 × 2 MMI after the interaction region to serve as the splitter/combiner at the output of the MZM. Now, moving from a peak to null bias condition will shift the light from one output port to another rather than exciting unwanted substrate modes. The addition of linear tapers on the input and output of the MMI further prevents reflections cause by MFD mismatch between the multimode region and the waveguides leading to substrate

modes. Moreover, because the optical mode is primarily confined in the LiNbO$_3$ slab, the multimode region of the 2 × 2 MMI must be relatively long compared to Silicon on Insulator (SOI) or silicon on LiNbO$_3$ strip-loaded waveguides, which maintain a higher index contrast than SiN$_x$ on LiNbO$_3$. As such, the LiNbO$_3$-SiN$_x$ material system affords greater fabrication tolerance, where, for example, a +/− 25 nm variation in the length of the multimode region is only .004% of the total length.

To demonstrate the ability of our 2 × 2 MMI to improve the extinction ratio of the MZM, we have measured the extinction ratio of the device under forward and reverse operation. In forward operation, light enters the device through the input port as defined in Fig. 1. (b), is split into two paths using a 1 × 2 MMI, and then is recombined after passing through the interaction region using a 2 × 2 MMI. Thermo-optic phase shifters, shown in Fig. 12 are used to sweep the bias condition of the device, and the peak and null intensity of each output port is collected on an Optical Spectrum Analyzer (OSA). The optical response of port 1 at peak and null bias is plotted in Fig. 8. (a) and (b), respectively. The optical response of port 2 at peak and null bias is plotted in Fig. 8. (d) and (c), respectively.

To validate these results, the optical transmission in is then collected using an optical power meter, and plotted to find the static extinction ratio of the device as the bias condition is swept through null bias for each output port, shown in Fig. 8. (c) and (f), corresponding to output ports 1 and 2, respectively. Multiple devices were measured to confirm the repeatability of this result. The optical power meter shows a higher ER than the OSA. To avoid misrepresentation of data, the lower number acquired from the OSA is used.

The same experiment is then performed with the device in reverse operation. Here, the laser source is connected to
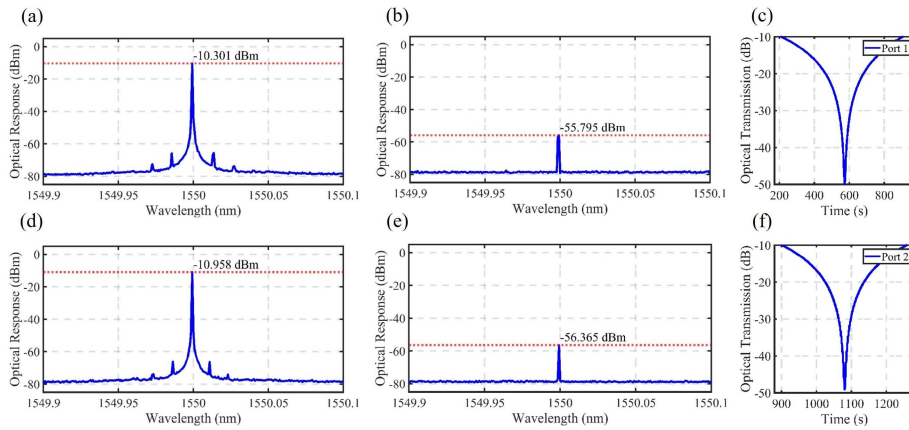
FIGURE 8. (a) Port 1 optical power output at respective peak bias while forward propagating through the modulator. (b) Port 1 optical power output at respective null bias while forward propagating through the modulator. (c) Port 1 optical power output while the bias condition is swept through respective null. (d) Port 2 optical power output at respective peak bias while forward propagating through the modulator. (e) Port 2 optical power output at respective null bias while forward propagating through the modulator. (f) Port 2 optical power output while the bias condition is swept through respective null. Data collected using an APEX Optical Spectrum Analyzer and Thor Labs handheld power meter. Input power is 1 mW, input and output fibers are separated from end facets to increase measurement stability. Peak power is not representative of total insertion loss.
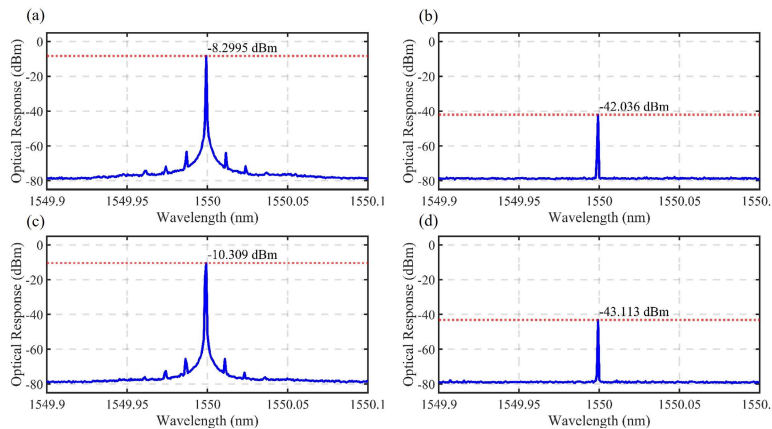

FIGURE 9. (a) Power output of the modulator at peak bias when fed backwards through output port 1. (b) Power output of the modulator at null bias when fed backwards through output port 1. (c) Power output of the modulator at peak bias when fed backwards through output port 2. (d) Power output of the modulator at null bias when fed backwards through output port 2. Data collected using an Optical Spectrum Analyzer. Input power is 1 mW, input and output fibers are separated from end facets to increase measurement stability. Peak power is not representative of total insertion loss.

either output port 1 or 2 as defined in Fig. 1. (b). Now, the 1×2 MMI splitter at the input acts as a 2×1 MMI combiner [25], [43], [45]. Thermo-optic phase shifters are again used to sweep the bias condition of the device, and the peak and null intensity of the output is collected on an OSA. The extinction ratio is measured using both ports 1 and 2 as the input and plotted in Fig. 9. The optical response of the device when fed from port 1 is plotted in Fig. 9. (a) and (b), respectively. The optical response of the device when fed from port 2 is plotted in Fig. 9. (c) and (d), respectively.

The extinction ratio of the device in forward operation is roughly 45 dB, while the extinction ratio of the device in

reverse operation is roughly 33 dB. This demonstrates the effectiveness of the 2×2 MMI in this material system, where a 45 dB extinction ratio is achieved without the need for cascaded directional couplers.

A 2×2 MMI transfer matrix is used to simulate the result after the fact to find the input power and splitting imbalance errors. The transfer matrix for this is shown below:

$$\begin{bmatrix} A' \\ B' \end{bmatrix} = e^{j\phi_0} \begin{bmatrix} 1 & e^{j\frac{\pi}{2}(\phi_{imbal})} \\ e^{j\frac{\pi}{2}(\phi_{imbal})} & 1 \end{bmatrix} \begin{bmatrix} Ae^{j\phi_A} \\ Be^{j\phi_B} \end{bmatrix} \begin{bmatrix} P_{imbal} \\ 1 \end{bmatrix}. \quad (3)$$

Here, A and B are the input power of both input ports while A' and B' represent the output power of the MMI
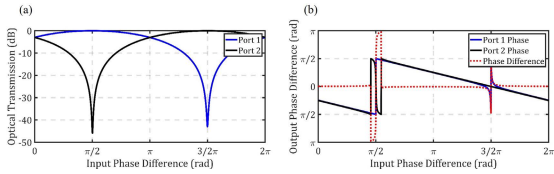
FIGURE 10. (a) Calculated extinction ratio from each port in the 2 × 2 MMI with applied splitting imbalance and input power imbalance. (b) Calculated relative phase relation from each port in the 2 × 2 MMI with applied splitting imbalance and input power imbalance.

FIGURE 11. (a) Measured optical sidebands and simulated EO response at quadrature bias from 0 to 40 GHz using a 1550 nm wavelength carrier signal. Measurement taken at output port 1, UV15 index matching fluid present. (b) Measured optical sidebands and simulated EO response at quadrature bias from 0 to 40 GHz using a 1550 nm wavelength carrier signal. Measurement taken at output port 2, UV15 index matching fluid present.

output ports. The term ϕ_0 is the constant phase offset that the MMI imparts on the optical mode. The $\pi/2$ term accounts for the ideal $\pi/2$ phase offset between the output ports when the MMI is fed by one input port. The term ϕ_{imbal} accounts for any discrepancies between the ideal $\pi/2$ phase offset and the actual phase offset, which may be different due to fabrication tolerances or design issues. Similarly, the term P_{imbal} accounts for unequal splitting within the MMI. With this, the output power of output ports A' and B', is

$$A' = e^{j\phi_0}\left(P_{imbal}Ae^{j\phi_A} + Be^{j\phi_B}e^{j\frac{\pi}{2}\phi_{imbal}}\right) \quad (4)$$

$$B' = e^{j\phi_0}\left(P_{imbal}Ae^{j\phi_A}e^{j\frac{\pi}{2}\phi_{imbal}} + Be^{j\phi_B}\right). \quad (5)$$

Using values $P_{imbal} = 0.998$, $\phi_{imbal} = 0.998$, $A = 1$, $B = 0.988$, the ER and phase relations of the 2 × 2 MMI are calculated and plotted in Fig. 10. (a) and (b), respectively. It is shown that this aligns well with the measured data and demonstrates that the 2 × 2 MMI will still produce a high ER when input power and splitting ratio are not perfectly balanced. If fabrication issues are expected, an additional thermal heater can be placed on the top or bottom of the MMI to tune the optical splitting ratio and account for fabrication errors [47]. Finally, the MMI can maintain a over 40 dB ER across the optical C-band, where a peak splitting difference of 1.4% is found at 1530 nm.

E. HIGH FREQUENCY EO RESPONSE
The traveling-wave electro-optic response of the MZM is achieved by measuring the optical sideband power with an RF modulating signal applied to the electrodes. A tunable telecom laser is used to launch 1550nm TE-polarized light into the device, while an RF signal generated by a signal generator is connected to the input side of the GSG electrode through a GSG probe so the RF and optical signals are co-propagating. In this way, the overlap between the modulating RF field and the modulated optical signal is maintained for as long as possible. The modulator is biased to quadrature using a DC current source connected to the TO phase shifters to ensure the modulator is operating in the most linear region of the response curve. The RF modulating signal is swept from 1 to 40 GHz in 1 GHz increments, and the intensity of the sidebands of the modulated optical signal is observed using an OSA [48]. The RF source is then connected to an RF thermocouple power meter and again
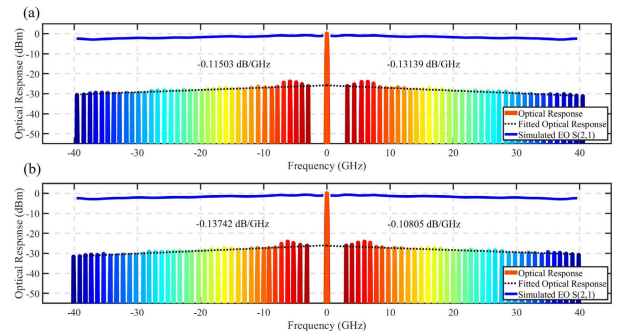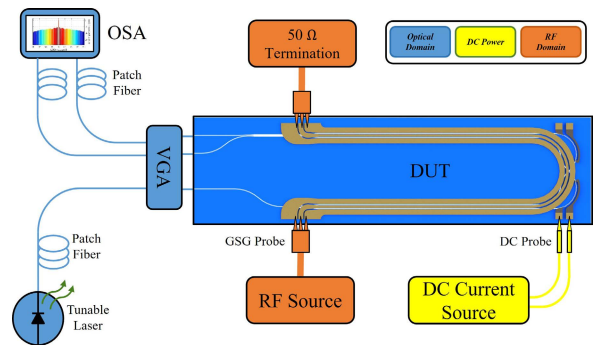

FIGURE 12. Schematic of the experimental setup used to collect sideband data of the device.

swept from 1 to 40 GHz to gather the RF input power at each frequency step. The modulation spectrum is normalized to the optical carrier input and RF power. The modulation spectrum of port 1 and 2 from 3 to 40 GHz at quadrature bias of the UV15-clad device is shown in Fig. 11. (a) and (b), respectively. Lower frequencies are omitted due to an unlevel power output from the RF source. The sideband power roll-off from low frequencies to 40 GHz is roughly 0.1 dB/GHz, excluding spurious low-frequency response, the 3 dB bandwidth is roughly 30 GHz. The experimental test setup is shown in Fig. 12. The measured EO response is a close match to the simulated EO response extracted from the measured electrical scattering matrix [49]. This confirms that the expected optical group index is accurate, where if it was not, there would be a discrepancy between the simulated and measured result.

V. CONCLUSION
In this work, a high extinction ratio hybrid LiNbO$_3$-SiN$_x$ electro-optic MZM with two equal and opposite outputs is designed, fabricated and characterized. The device uses a 2 × 2 MMI at the output to provide two inversely proportional outputs with exceptional extinction ratio performance.

Fiber couplers are used at the input and output to lower the total insertion loss to 12 dB. To the best of our knowledge, this is the first time a high extinction ratio, folded, dual output LiNbO$_3$-SiN$_x$ electro-optic dual-output MZM with a waveguide crossing has been demonstrated in this material platform. The device presented shows a measured DC-Vπ of 3.0 V with an 11 mm interaction region, and an extinction ratio of over 45 dB. This design does not require cascaded directional couplers to control splitting imbalance, and shows repeatability across multiple devices. This is nearly 31 times higher than high-extinction ratio single-output modulators in literature today. There is a clear path forward to optimizing either or both the low and high frequency operation depending on application-specific requirements. In future work, capacitively-loaded traveling-wave electrodes will be incorporated to increase the operational bandwidth.

A dual-output MZM can be paired with a balanced PD receiver and used in many photonic communication systems where a high extinction, dual output device is paramount to the high-performance operation of the system as a whole. This enables heavy, lossy and space-consuming cables to be replaced with much lighter optical fibers. A balanced PD receiver pair is capable of detecting both the signal amplitude and phase information and is compatible with complex modulation formats used in DPSK and DQPSK systems. Moreover, the demonstration of the 2×2 MMI coupler to reach >45 dB ER lends itself to exotic applications such as IR and mid-IR Bracewell nulling interferometry for exoplanet detection [50].

ACKNOWLEDGMENT

REFERENCES

[1] A. Alvarado, D. J. Ives, S. J. Savory, and P. Bayvel, "On the impact of optimal modulation and FEC overhead on future optical networks," *J. Lightw. Technol.*, vol. 34, no. 9, pp. 2339–2352, May 1, 2016.

[2] P. J. Winzer and D. T. Neilson, "From scaling disparities to integrated parallelism: A decathlon for a decade," *J. Lightw. Technol.*, vol. 35, no. 5, pp. 1099–1115, Mar. 2017.

[3] Q. Cheng, M. Bahadori, M. Glick, S. Rumley, and K. Bergman, "Recent advances in optical technologies for data centers: A review," *Optica*, vol. 5, no. 11, p. 1354, Nov. 2018.

[4] Y. Yue, Q. Wang, and J. Anderson, "Experimental investigation of 400 Gb/s data center interconnect using unamplified high-baud-rate and high-order QAM single-carrier signal," *Appl. Sci.*, vol. 9, no. 12, p. 2455, Jun. 2019.

[5] E. L. Wooten, K. M. Kissa, A. Yi-Yan, E. J. Murphy, D. A. Lafaw, P. F. Hallemeier, D. Maack, D. V. Attanasio, D. J. Fritz, G. J. McBrien, and D. E. Bossi, "A review of lithium niobate modulators for fiber-optic communications systems," *IEEE J. Sel. Topics Quantum Electron.*, vol. 6, no. 1, pp. 69–82, Jan. 2000.

[6] V. A. Carey, M. R. Konkol, S. Shi, A. J. Mercante, K. Shreve, A. A. Wright, C. A. Schuetz, and D. W. Prather, "Millimeter wave photonic tightly coupled array," *IEEE Trans. Antennas Propag.*, vol. 69, no. 8, pp. 4488–4503, Aug. 2021.

[7] W. Beardell, B. Mazur, C. Ryan, G. Schneider, J. Murakowski, and D. Prather, "RF-photonic spatial–spectral channelizing receiver," *J. Lightw. Technol.*, vol. 40, no. 2, pp. 432–441, Jan. 15, 2022.

[8] S. Nelan, A. Mercante, C. Hurley, S. Shi, P. Yao, B. Shopp, and D. W. Prather, "Compact thin film lithium niobate folded intensity modulator using a waveguide crossing," *Opt. Exp.*, vol. 30, no. 6, p. 9193, Mar. 2022.

[9] Y. Liu, H. Li, J. Liu, S. Tan, Q. Lu, and W. Guo, "Low Vπ thin-film lithium niobate modulator fabricated with photolithography," *Opt. Exp.*, vol. 29, no. 5, p. 6320, Mar. 2021.

[10] G. Chen, K. Chen, R. Gan, Z. Ruan, Z. Wang, P. Huang, C. Lu, A. P. T. Lau, D. Dai, C. Guo, and L. Liu, "High performance thin-film lithium niobate modulator on a silicon substrate using periodic capacitively loaded traveling-wave electrode," *APL Photon.*, vol. 7, no. 2, Feb. 2022, Art. no. 026103.

[11] X. Zhang, C.-J. Chung, A. Hosseini, H. Subbaraman, J. Luo, A. K.-Y. Jen, R. L. Nelson, C. Y.-C. Lee, and R. T. Chen, "High performance optical modulator based on electro-optic polymer filled silicon slot photonic crystal waveguide," *J. Lightw. Technol.*, vol. 34, no. 12, pp. 2941–2951, Jun. 2016.

[12] M. Zhang, C. Wang, P. Kharel, D. Zhu, and M. Lončar, "Integrated lithium niobate electro-optic modulators: When performance meets scalability," *Optica*, vol. 8, no. 5, p. 652, May 2021.

[13] M. He, M. Xu, Y. Ren, J. Jian, Z. Ruan, Y. Xu, S. Gao, S. Sun, X. Wen, L. Zhou, L. Liu, C. Guo, H. Chen, S. Yu, L. Liu, and X. Cai, "High-performance hybrid silicon and lithium niobate Mach–Zehnder modulators for 100 Gbit s^{-1} and beyond," *Nature Photon.*, vol. 13, no. 5, pp. 359–364, May 2019.

[14] A. N. R. Ahmed, S. Shi, A. Mercante, S. Nelan, P. Yao, and D. W. Prather, "High-efficiency lithium niobate modulator for K band operation," *APL Photon.*, vol. 5, no. 9, Sep. 2020, Art. no. 091302.

[15] A. J. Mercante, S. Shi, P. Yao, L. Xie, R. M. Weikle, and D. W. Prather, "Thin film lithium niobate electro-optic modulator with terahertz operating bandwidth," *Opt. Exp.*, vol. 26, no. 11, p. 14810, May 2018.

[16] A. Rao and S. Fathpour, "Compact lithium niobate electrooptic modulators," *IEEE J. Sel. Topics Quantum Electron.*, vol. 24, no. 4, pp. 1–14, Jul. 2018.

[17] G. T. Reed, G. Mashanovich, F. Y. Gardes, and D. J. Thomson, "Silicon optical modulators," *Nature Photon.*, vol. 4, no. 8, pp. 518–526, Aug. 2010.

[18] P. O. Weigel, J. Zhao, K. Fang, H. Al-Rubaye, D. Trotter, D. Hood, J. Mudrick, C. Dallo, A. T. Pomerene, A. L. Starbuck, C. T. DeRose, A. L. Lentine, G. Rebeiz, and S. Mookherjea, "Bonded thin film lithium niobate modulator on a silicon photonics platform exceeding 100 GHz 3-dB electrical modulation bandwidth," *Opt. Exp.*, vol. 26, no. 18, p. 23728, Sep. 2018.

[19] F. Horst, W. M. J. Green, S. Assefa, S. M. Shank, Y. A. Vlasov, and B. J. Offrein, "Cascaded Mach–Zehnder wavelength filters in silicon photonics for low loss and flat pass-band WDM (de-)multiplexing," *Opt. Exp.*, vol. 21, no. 10, p. 11652, May 2013.

[20] D. Huo, Z. J. Choong, Y. Shi, J. Hedley, and Y. Zhao, "Diamond micromilling of lithium niobate for sensing applications," *J. Micromech. Microeng.*, vol. 26, no. 9, Sep. 2016, Art. no. 095005.

[21] C. Wang, M. Zhang, X. Chen, M. Bertrand, A. Shams-Ansari, S. Chandrasekhar, P. Winzer, and M. Loncar, "Integrated lithium niobate electro-optic modulators operating at CMOS-compatible voltages," *Nature*, vol. 562, no. 7725, pp. 101–104, Oct. 2018.

[22] L. Alloatti, R. Palmer, S. Diebold, K. P. Pahl, B. Chen, R. Dinu, M. Fournier, J.-M. Fedeli, T. Zwick, W. Freude, C. Koos, and J. Leuthold, "100 GHz silicon–organic hybrid modulator," *Light, Sci. Appl.*, vol. 3, no. 5, p. e173, May 2014.

[23] C. Haffner, W. Heni, Y. Fedoryshyn, J. Niegemann, A. Melikyan, D. L. Elder, B. Baeuerle, Y. Salamin, A. Josten, U. Koch, C. Hoessbacher, F. Ducry, L. Juchli, A. Emboras, D. Hillerkuss, M. Kohl, L. R. Dalton, C. Hafner, and J. Leuthold, "All-plasmonic Mach–Zehnder modulator enabling optical high-speed communication at the microscale," *Nature Photon.*, vol. 9, no. 8, pp. 525–528, Aug. 2015.

[24] J. F. Coward, C. H. Chalfant, and P. H. Chang, "A photonic integrated-optic RF phase shifter for phased array antenna beam-forming applications," *J. Lightw. Technol.*, vol. 11, no. 12, pp. 2201–2205, Dec. 1993.

[25] A. N. R. Ahmed, S. Nelan, S. Shi, P. Yao, A. Mercante, and D. W. Prather, "Subvolt electro-optical modulator on thin-film lithium niobate and silicon nitride hybrid platform," *Opt. Lett.*, vol. 45, no. 5, p. 1112, Mar. 2020.

[26] M. Jin, J.-Y. Chen, Y. M. Sua, and Y.-P. Huang, "High-extinction electro-optic modulation on lithium niobate thin film," *Opt. Lett.*, vol. 44, no. 5, p. 1265, Mar. 2019.

[27] X. Wang, C. Shang, A. Pan, X. Cheng, T. Gui, S. Yuan, C. Gui, K. Zheng, P. Zhang, X. Song, Y. Li, L. Li, C. Zeng, and J. Xia, "Thin-film lithium niobate based dual-polarization IQ modulator for single-carrier 1.6 Tb/s transmission," *Proc. SPIE*, vol. 12004, pp. 87–90, Mar. 2022.

[28] H. Subbaraman, X. Xu, A. Hosseini, X. Zhang, Y. Zhang, D. Kwong, and R. T. Chen, "Recent advances in silicon-based passive and active optical interconnects," *Opt. Exp.*, vol. 23, no. 3, p. 2487, Feb. 2015.

[29] S. S. Azadeh, F. Merget, S. Romero-García, A. Moscoso-Mártir, N. von den Driesch, J. Müller, S. Mantl, D. Buca, and J. Witzens, "Low Vπ silicon photonics modulators with highly linear epitaxially grown phase shifters," *Opt. Exp.*, vol. 23, no. 18, p. 23526, Sep. 2015.

[30] M. Dinu, F. Quochi, and H. Garcia, "Third-order nonlinearities in silicon at telecom wavelengths," *Appl. Phys. Lett.*, vol. 82, no. 18, pp. 2954–2956, May 2003.

[31] M.-C. Oh, H. Zhang, C. Zhang, H. Erlig, Y. Chang, B. Tsap, D. Chang, A. Szep, W. H. Steier, H. R. Fetterman, and L. R. Dalton, "Recent advances in electrooptic polymer modulators incorporating highly nonlinear chromophore," *IEEE J. Sel. Topics Quantum Electron.*, vol. 7, no. 5, pp. 826–835, Sep./Oct. 2001.

[32] C. Wang, M. Zhang, B. Stern, M. Lipson, and M. Lončar, "Nanophotonic lithium niobate electro-optic modulators," *Opt. Exp.*, vol. 26, no. 2, p. 1547, Jan. 2018.

[33] A. Rao, A. Patil, P. Rabiei, A. Honardoost, R. DeSalvo, A. Paolella, and S. Fathpour, "High-performance and linear thin-film lithium niobate Mach–Zehnder modulators on silicon up to 50 GHz," *Opt. Lett.*, vol. 41, no. 24, p. 5700, Dec. 2016.

[34] T. A. Huffman, G. M. Brodnik, C. Pinho, S. Gundavarapu, D. Baney, and D. J. Blumenthal, "Integrated resonators in an ultralow loss Si_3N_4/SiO_2 platform for multifunction applications," *IEEE J. Sel. Topics Quantum Electron.*, vol. 24, no. 4, pp. 1–9, Jul. 2018.

[35] S. Jin, L. Xu, H. Zhang, and Y. Li, "$LiNbO_3$ thin-film modulators using silicon nitride surface ridge waveguides," *IEEE Photon. Technol. Lett.*, vol. 28, no. 7, pp. 736–739, Apr. 1, 2016.

[36] M. Stocchi, D. Mencarelli, L. Pierantoni, D. Kot, M. Lisker, A. Göritz, C. B. Kaynak, M. Wietstruck, and M. Kaynak, "Mid-infrared optical characterization of thin SiN_x membranes," *Appl. Opt.*, vol. 58, no. 19, p. 5233, Jul. 2019.

[37] A. E. Kaloyeros, F. A. Jové, J. Goff, and B. Arkles, "Review—Silicon nitride and silicon nitride-rich thin film technologies: Trends in deposition techniques and related applications," *ECS J. Solid State Sci. Technol.*, vol. 6, no. 10, pp. P691–P714, 2017.

[38] S. Sun, M. Xu, M. He, S. Gao, X. Zhang, L. Zhou, L. Liu, S. Yu, and X. Cai, "Folded heterogeneous silicon and lithium niobate Mach–Zehnder modulators with low drive voltage," *Micromachines*, vol. 12, no. 7, p. 823, Jul. 2021.

[39] J. Hu, C. Li, C. Guo, C. Lu, A. P. T. Lau, P. Chen, and L. Liu, "Folded thin-film lithium niobate modulator based on a poled Mach–Zehnder interferometer structure," *Opt. Lett.*, vol. 46, no. 12, pp. 2940–2943, Jun. 2021.

[40] F. Zhang, Y. Qi, and W. Li, "Using optical differential phase-shift keying to solve the bipolarity problem of spreading code in optical time domain reflectometer," *Results Phys.*, vol. 13, Jun. 2019, Art. no. 102096.

[41] T. Ren, M. Zhang, C. Wang, L. Shao, C. Reimer, Y. Zhang, O. King, R. Esman, T. Cullen, and M. Loncar, "An integrated low-voltage broadband lithium niobate phase modulator," *IEEE Photon. Technol. Lett.*, vol. 31, no. 11, pp. 889–892, Jun. 1, 2019.

[42] X. Jin, J. Su, Y. Zheng, C. Chen, W. Wang, and K. Peng, "Balanced homodyne detection with high common mode rejection ratio based on parameter compensation of two arbitrary photodiodes," *Opt. Exp.*, vol. 23, no. 18, p. 23859, Sep. 2015.

[43] D. Khalil and A. Yehia, "Two-dimensional multimode interference in integrated optical structures," *J. Opt. A, Pure Appl. Opt.*, vol. 6, no. 1, pp. 137–145, Jan. 2004.

[44] M. Bachmann, P. A. Besse, and H. Melchior, "General self-imaging properties in N×N multimode interference couplers including phase relations," *Appl. Opt.*, vol. 33, no. 18, pp. 3905–3911, Jun. 1994.

[45] J. Wang, M. Qi, Y. Xuan, H. Huang, Y. Li, M. Li, X. Chen, Q. Jia, Z. Sheng, A. Wu, W. Li, X. Wang, S. Zou, and F. Gan, "Proposal for fabrication-tolerant SOI polarization splitter-rotator based on cascaded MMI couplers and an assisted bi-level taper," *Opt. Exp.*, vol. 22, no. 23, p. 27869, Nov. 2014.

[46] J. A. I. Fuste and M. C. S. Blanco, "Bandwidth–length trade-off figures of merit for electro-optic traveling wave modulators," *Opt. Lett.*, vol. 38, no. 9, p. 1548, May 2013.

[47] Á. Rosa, A. Brimont, A. Griol, and P. Sanchis, "High performace silicon 2 × 2 optical switch based on a thermo-optically tunable multimode interference coupler and efficient electrodes," *Opt. Exp.*, vol. 24, no. 1, pp. 191–198, Jan. 2016.

[48] Y. Shi, L. Yan, and A. E. Willner, "High-speed electrooptic modulator characterization using optical spectrum analysis," *J. Lightw. Technol.*, vol. 21, no. 10, p. 2358, Oct. 2003.

[49] D. Zhu, L. Shao, M. Yu, R. Cheng, B. Desiatov, C. J. Xin, Y. Hu, J. Holzgrafe, S. Ghosh, A. Shams-Ansari, E. Puma, N. Sinclair, C. Reimer, M. Zhang, and M. Lončar, "Integrated photonics on thin-film lithium niobate," *Adv. Opt. Photon.*, vol. 13, no. 2, pp. 242–352, Jun. 2021.

[50] H.-D. K. Goldsmith, N. Cvetojevic, M. Ireland, and S. Madden, "Fabrication tolerant chalcogenide mid-infrared multimode interference coupler design with applications for Bracewell nulling interferometry," *Opt. Exp.*, vol. 25, no. 4, pp. 3038–3051, Feb. 2017.

SEAN P. NELAN received the B.S. degree in electrical engineering from the University of Delaware, Newark, DE, USA, in 2018, and the Ph.D. degree in electromagnetics and photonics, in 2022. He is currently conducting a Postdoctoral Research at Phase Sensitive Innovations Inc., where his works include the design, development, and fabrication of thin-film lithium niobate devices, and device layout with a focus on high-performance electro-optic modulators.

ANDREW MERCANTE received the B.S. degree in electrical engineering from the University of Delaware, Newark, DE, USA, in 2013, and the Ph.D. degree, in 2018. His focus is on the design and fabrication of ultra-wideband electro-optic phase modulators in thin-film lithium niobate. He is currently conducting a Postdoctoral Research at Phase Sensitive Innovations Inc., where his research interests include further development of thin-film lithium niobate devices and heterogeneous integration of materials.

SHOUYUAN SHI received the B.S., M.S., and Ph.D. degrees from Xidian University, Xi'an, China, in 1991, 1994, and 1997, respectively, all in electrical engineering. He is currently a Research Professor with the Department of Electrical and Computer Engineering, University of Delaware, Newark, DE, USA. His research interests include computational electromagnetics, microoptics and nanophotonics, and RF-photonics technologies and applications, including ultra-wideband RF antennas, optically addressed phase arrays, ultra-wideband electro-optic devices and systems, and passive and active millimeter wave imaging systems. He is the author or a coauthor of eight books and book chapters, and more than 380 peer refereed journals and conference publications. He holds over 20 issued U.S. patents and ten provisional patents. He is also served as the Topic Editor for *Photonic Devices and Materials* and the *Optical and Photonic Letters*, and an Editorial Board Member for Advanced Optics. He is also an active reviewer for more than 20 international peer-reviewed journals in the research areas of optics and photonics, RF, electro-optics, and electromagnetics.

PENG YAO received the B.S. and M.S. degrees from the Department of Mechanical Engineering, Xi'an Jiaotong University, China, in 1998 and 2001, respectively, and the Ph.D. degree in the area of nano and micro fabrication of electronic and optical devices from the Graduate School, University of Delaware, in 2007. He holds two issued U.S. patents and seven provisional patents. He is the author or coauthor of one book chapter and over 50 peer reviewed journals and international conference papers. He joined Phase Sensitive Innovations, in 2007, as the Lead Engineer in new component Research and Development and is responsible for the development of the world leading LN modulator products and high-power photodiode products. His current research interests include broadband LN or LNOI modulators, high-speed and high power photodiodes, packaging of high frequency passive and active components, microwave photonic links, micro fabrication techniques, and passive and active millimeter wave imaging systems.

ELIEZER SHAHID received the B.S. degree in electrical engineering from the University of Delaware, in 2021. He is currently working on the development of thin-film lithium niobate photonic devices at Phase Sensitive Innovations Inc., with a focus on new fabrication techniques for the realization of high-performance electro-optic modulators.

BENJAMIN A. SHOPP received the bachelor's degree in electrical engineering from the University of Delaware, Newark, DE, USA, in 2020. After completing his bachelor's degree, he has been performing research with Phase Sensitive Innovations Inc., focusing on optical testing/integration, development, and fabrication of thin-film lithium niobate devices.

COOPER D. HURLEY received the bachelor's degree in electrical engineering from the University of Delaware, Newark, DE, USA, in 2018, and the M.S. degree in electromagnetics and photonics, in 2022. He has performed research in a wide field of topics, including electromagnetic and photonic device design, simulation and layout, and light-emitting diode design, layout, and PCB design and fabrication.

MATHEW ZABLOCKI received the B.S. degree in physics from West Chester University, in 2007, and the Ph.D. degree in electrical engineering from the University of Delaware, in 2012. He is currently the Director of Photonic Applications at Phase Sensitive Innovations. He has four patents for photonic devices and is the coauthor for a book chapter. He has lead as a Primary Investigator on two SBIR Phase II efforts and contributed to several SBIR and STTR efforts. A large focus within his research was the development of semiconductor-based optical interconnects. His work required many efforts in process development of tight tolerance photonics devices, achieving state-of-the-art performance in silicon photonic propagation losses and signal isolation. His research interests include the development of processing that provides a means to transfer photonics devices and materials to secondary planar and non-planar surfaces, of which he holds a patent. His work continues in increasing performance and the manufacturing readinss level of next-generation lithium niobate modulators.

DENNIS W. PRATHER received the B.S.E.E., M.S.E.E., and Ph.D. degrees from the University of Maryland. He began his professional career by joining the U.S. Navy, where he served as an Engineering Duty Officer. He is currently the College of Engineering Endowed Alumni Distinguished Professor with the Department of Electrical and Computer Engineering, University of Delaware. His research interests include RF-photonic devices, analog photonic integrated circuits, optical processing components, and their application to various systems for see-through imaging, wireless and digital communications, and navigational radar.

• • •